

Insulator to semimetallic transition in conducting polymersW. A. Muñoz,^{1,*} Sandeep Kumar Singh,¹ J. F. Franco-Gonzalez,¹ M. Linares,^{2,3} X. Crispin,¹ and I. V. Zozoulenko^{1,†}¹Laboratory of Organic Electronics, ITN, Linköping University, 601 74 Norrköping, Sweden²Department of Physics, Chemistry and Biology, IFM, Linköping University, 581 83 Linköping, Sweden³Swedish e-Science Research Centre (SeRC), Linköping University, 581 83 Linköping, Sweden

(Received 5 July 2016; revised manuscript received 10 October 2016; published 17 November 2016)

We report a multiscale modeling of electronic structure of a conducting polymer poly(3,4-ethylenedioxythiophene) (PEDOT) based on a realistic model of its morphology. We show that when the charge carrier concentration increases, the character of the density of states (DOS) gradually evolves from the insulating to the semimetallic, exhibiting a collapse of the gap between the bipolaron and valence bands with the drastic increase of the DOS between the bands. The origin of the observed behavior is attributed to the effect of randomly located counterions giving rise to the states in the gap. These results are discussed in light of recent experiments. The method developed in this work is general and can be applied to study the electronic structure of other conducting polymers.

DOI: [10.1103/PhysRevB.94.205202](https://doi.org/10.1103/PhysRevB.94.205202)**I. INTRODUCTION**

Conductive polymers exhibiting novel properties typically not available in inorganic materials constitute a cornerstone for a new promising technological platform for electronic devices [1–3]. Nowadays, poly(3,4-ethylenedioxythiophene) or PEDOT has been the most studied conducting polymer due its high electronic (hole) conductivity (1000–4000 S/cm) [4–6], room-temperature stability [7], and remarkable thermoelectric properties with the highest figure of merit for organic materials [8–11]. Given the temperature dependence of conductivity σ (σ increases with the temperature T) and the high degree of inherent disorder, it is generally accepted that the transport in doped conductive polymers is mediated by phonon-assisted hopping between the localized states [12–18]. These states are associated with singly (polaron) or doubly (bipolaron) positively charged defects (geometrical distortion of the chains) forming due to the strong electron-phonon coupling. The polarons or bipolarons are balanced by the negative counterions introduced during the synthesis.

During recent years, there has been tremendous activity aimed at understanding the electrical transport in PEDOT and its relationship with electronic structure and morphology [4,12–14,19,20]. Because the conductivity is directly related to the density of states (DOS) [14], one of the major challenges in understanding the transport properties can be traced back to the understanding of the DOS. It is remarkable that despite the fundamental importance of this issue, there has been no theory providing a microscopic description of the DOS in realistic PEDOT and related conducting polymers.

The challenge of the description of electronic properties of realistic polymeric thin films is that it requires multiscale modeling, encompassing an angstrom scale defining the nature of charged states (bipolarons or polarons) and nanometer scale representing the complex morphology of the system at hand. Besides, this task requires approaches capable of calculating the electronic properties of systems consisting of hundreds

or thousands of atoms, which far exceeds the capabilities of standard quantum-mechanical packages. So far, the electronic properties of PEDOT and related conducting polymers have been studied on the basis of largely oversimplified models such as single polymeric chains [21–24] or infinite perfect periodic crystals [25–27]. None of these models are in a position to capture the morphology and the DOS of realistic PEDOT thin films. In the absence of theoretical models, researchers usually rely on phenomenological models for DOS such as Gaussian or exponential disorder [13,28].

Recently, Bubnova *et al.* [4] reported a semimetallic behavior in PEDOT as manifested in its electrical conductivity and thermopower. The authors speculated about the possible evolution of the band structure, suggesting that the bipolaron band merges into the delocalized valence band, but no theory explaining this remarkable behavior has been proposed so far.

In this paper, we provide a microscopic description of the band structure and the DOS of realistic PEDOT based on the multiscale modeling using *ab initio*, molecular dynamics, and semiempirical calculations. Note that even though the calculations are performed for PEDOT, our results can be used to understand the trends in the electronic structure of other widely studied conducting polymers, such as polythiophenes and polyphenylene vinylene.

II. MODEL AND METHODS

In order to construct a realistic model of doped PEDOT thin films, it is important to understand the basic features of their morphology. Grazing incidence wide-angle x-ray scattering (GIWAXS) represents a powerful technique for the structural characterization of polymers [4,18,29,30]. An interpretation of the scattering pattern emerging from the GIWAXS measurements is that the PEDOT films are polycrystals consisting of (mono)crystallites embedded in an amorphous matrix. A broadening of the scattering peaks suggests that each crystallite typically consists of 3–15 π - π stacked PEDOT chains. In order to verify this picture, we performed molecular dynamics (MD) simulations of the PEDOT morphology. (A brief description of the MD simulations is given in Appendix A.) The MD simulations show that PEDOT chains are stacked in crystallites

*william.armando.munoz@liu.se

†igor.zozoulenko@liu.se

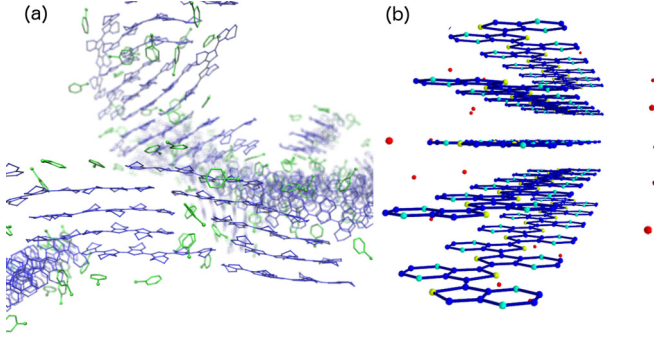


FIG. 1. (a) A representative morphological conformation of PEDOT (blue) with tosylate counterions (green) obtained from MD simulations. (b) A model of crystallite used in semiempirical calculations. The crystallite is composed of five π - π stacked PEDOT chains of the length of 12 monomer units. Negative point charge counterions (red) are randomly distributed around the crystallite.

surrounded by randomly distributed counterions; see Fig. 1(a). The crystallites are linked by interpenetrating PEDOT chains or π - π connections between chains belonging to different crystallites. This apparently leads to a formation of percolative paths through the whole crystal which can support a good conductivity.

Based on the GIWAXS data as well as on our MD simulations, we model the material as a polycrystal consisting of crystallites, as depicted in Fig. 1(b). Each crystallite is composed of five π - π stacked PEDOT chains of a finite length of 12 monomer units. The stacking configuration is obtained from the density functional theory (DFT) calculations. Concerning the nature of charge carriers (polarons vs bipolarons), for the case of PEDOT there is a clear evidence of the spinless character of carriers, indicating that doping occurs mostly via bipolarons with a negligible fraction of spin per monomer related to polarons (the latter has a spin 1/2) [4]. We create bipolarons in the crystallite by removing N_e electrons from the higher energy levels. To keep the electroneutrality, N_e negative point charge counterions $-e$ are randomly distributed around the crystallite. The band structure of the polycrystalline PEDOT is obtained by averaging of the DOS over many crystallites corresponding to different configurations of counterions (typically 1000 samples).

Since a size of a crystallite is prohibitively large for the DFT calculations, we calculate the crystallite's band structure using a semiempirical Hamiltonian for interacting π electrons, which is parametrized using the DFT calculations and the experimental data for the PEDOT band-gap energy,

$$\mathcal{H} = \mathcal{H}_{el} + \mathcal{H}_{lat} + \mathcal{H}_{\pi-\pi} + \mathcal{H}_{e-e} + \mathcal{H}_{ion}. \quad (1)$$

The first two terms correspond to the Su-Schrieffer-Heeger (SSH) Hamiltonian for a single chain [31]; the electronic part is described by the standard tight-binding Hamiltonian:

$$\mathcal{H}_{el} = \sum_{i\sigma} \varepsilon_{0i}^A c_{i\sigma}^\dagger c_{i\sigma} - \sum_{ij\sigma} t_{ij} c_{i\sigma}^\dagger c_{j\sigma} + \text{H.c.}, \quad (2)$$

where $c_{i\sigma}^\dagger$ and $c_{i\sigma}$ are the creation and annihilation operators at the site i with the spin σ , and the hopping integral is defined by the semiempirical relation $t_{ij} = t_0 \exp[-\alpha(u_{ij} - u_{ij}^0)]$ with

$t_0 = 2.46$ eV, $u_{ij} = |\mathbf{r}_i - \mathbf{r}_j|$ is the bond length between the nearest neighbors i th and j th atoms, while u_{ij}^0 are the interatomic distances at equilibrium ($u_{ij}^0 = 1.56, 1.78,$ and 1.43 Å for, respectively, C-C, C-S, and C-O atoms). ε_{0i}^A is the on-site energy on site i ($\varepsilon_{0i}^A = 0, -2.85,$ and -5.46 eV with A corresponding to C, S, or O atoms). The electron-phonon coupling is

$$\mathcal{H}_{lat} = \sum_{ij} K_{ij} (u_{ij} - u_{ij}^0 + \alpha^{-1}), \quad (3)$$

where $\alpha = 2.9$ Å⁻¹, and the spring constant $K_{ij} = \beta t_{ij}$ is related to the hopping integral by the parameter $\beta = 7.71$ Å⁻¹.

The interchain hopping due to the π - π interaction is given by $H_{\pi-\pi} = -\sum_{ij'\sigma} t_{ij'}^{\pi-\pi} c_{i\sigma}^\dagger c_{j'\sigma} + \text{H.c.}$, where i and j' belong to different chains, and hopping integral $t_{ij'}^{\pi-\pi} = t_0^{\pi-\pi} \exp(\frac{r_{\pi-\pi} - |\mathbf{r}_i - \mathbf{r}_{j'}|}{\delta})$, where $t_0^{\pi-\pi} = 0.32$ eV is the interchain nearest-neighbor hopping integral. A cutoff for the interchain hopping is defined here as $r_{\text{cutoff}} = r_{\pi-\pi} + 5\delta$, with $r_{\pi-\pi} = 3.43$ Å being the π - π stacking distance, and $\delta = 0.45$ Å.

The electron-electron interaction is included by means of the extended Hubbard Hamiltonian,

$$\mathcal{H}_{e-e} = \frac{U_0}{2} \sum_{i\sigma} n_{i\sigma} n_{i\sigma'} + \frac{1}{2} \sum_{ij\sigma\sigma'} V_{ij} n_{i\sigma} n_{j\sigma'}, \quad (4)$$

where the operator $n_{i\sigma} = c_{i\sigma}^\dagger c_{i\sigma}$, and $U_0 = 2.2$ eV. We adopted a Hubbard-Ohno potential to model intersite electron-electron interaction, which is expressed according to [32,33]

$$V_{ij} = \frac{U_0 e^{-\gamma|r_{ij}/R_0|}}{\sqrt{1 + (r_{ij}/R_0)^2}}, \quad (5)$$

where r_{ij} is the interatomic distance between the i th and j th sites. The value of scale parameter R_0 is set to the averaged C-C distance $r_{C-C} = 1.38$ Å for the interacting orbitals in the same chain, and to $r_{\pi-\pi}$ for interaction between the orbitals in the adjacent chains.

The last term in the Hamiltonian (1) corresponds to the electrostatic potential due to the counterions, $\mathcal{H}_{ion} = \sum_{i\sigma} V_i^{\text{ion}} c_{i\sigma}^\dagger c_{i\sigma}$. The interaction between the counterions and the atomic orbital at the position \mathbf{r}_i is modeled by a screened Coulomb potential [32],

$$V_i^{\text{ion}} = -\frac{e^2}{4\pi\epsilon_0\epsilon} \sum_{j=1}^{N_e} \frac{1}{|\mathbf{r}_i - \mathbf{r}_j|} \times \begin{cases} 1, & |\mathbf{r}_i - \mathbf{r}_j| \leq 4r_{C-C} \\ e^{-\frac{\gamma|\mathbf{r}_i - \mathbf{r}_j|}{R_0}}, & \text{otherwise,} \end{cases} \quad (6)$$

where the summation is carried out over N_e counterions located at the random positions \mathbf{r}_j , and the relative permittivity of PEDOT is set to $\epsilon = 3.5$. [27]. The inter- and intrachain screening is, respectively, $\gamma^{\text{inter}} = 1.2$ and $\gamma^{\text{intra}} = 0.65$.

The chosen crystallite size corresponds to $N = 420$ atomic sites, thus giving rise to $2N$ energy levels for N π -electrons in each crystallite (factor 2 accounts for spin; each monomer contains seven π -electrons corresponding to four C atoms

TABLE I. Semiempirical parameters used for the electronic energy calculations of PEDOT.

u_{C-C}^0	u_{C-S}^0	u_{C-O}^0	ε_0^C	ε_0^S	ε_0^O		
1.56 Å	1.78 Å	1.43 Å	0 eV	-2.85 eV ^a	-5.46 eV ^a		
t_0	α	β	$t_0^{\pi-\pi}$	U_0	γ^{intra}	γ^{inter}	
2.46 eV	2.9 Å ⁻¹	7.71 Å ⁻¹	0.32 eV	2.2 eV	0.65	1.2	

^aRef. [34].

in the backbone, two S, and one O atom). We solve self-consistently for the Schrödinger equation with Hamiltonian (1) by minimizing the total energy with respect to the bond displacements u_{ij} . Details of the minimization procedure along with a description of a parametrization are provided in Appendices B and C, and the values of all parameters used in Eqs. (1)–(6) are listed in Table I.

III. RESULTS AND DISCUSSION

Figure 2 shows a band structure of a representative crystallite for different carrier concentrations $n_e = \frac{N_e}{N_{\text{mon}}}$, where N_{mon} is the total number of monomers in the crystallite. The lowest N_e unoccupied electron states correspond to the bipolaron band lying between the conduction and valence bands. The bipolaron band is formed by N_e states that are removed from the valence and conduction bands of the uncharged system $n_e = 0$ [Fig. 2(a)]. As the carrier concentration increases, more states are pulled into the bipolaron band. As a result, it becomes wider and the gap $E_g = E_{\text{LUMO}} - E_{\text{HOMO}}$ between the bipolaron and valence bands shrinks; cf. Figs. 2(b)–2(d). Figures 2(b) and 2(c) show the DOS of two crystallites with the same carrier concentration but for different sample realizations. The calculated DOS exhibits pronounced sample-to-sample variations related to the disordered character of the external electrostatic potential due to random counterions. It

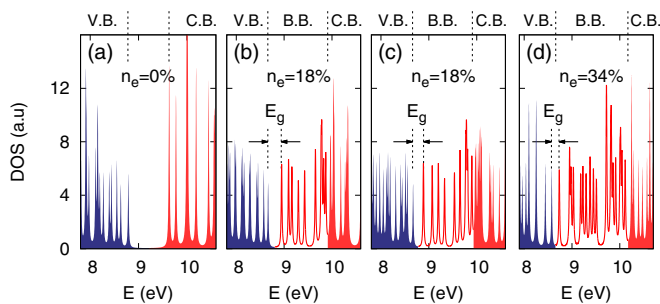


FIG. 2. DOS of representative crystallites for different carrier concentrations (a) $n_e = 0\%$, (b),(c) $n_e = 18\%$, and (d) $n_e = 34\%$. (For visualization purposes, each level is plotted as a Lorentzian with a finite width.) Note that (b) and (c) correspond to the same n_e but different counterion realizations. Blue and red peaks correspond to occupied and unoccupied electronic states, respectively. V.B., C.B., and B.B. correspond to valence, conduction, and bipolaron bands, respectively. States in the B.B. and C.B. are plotted as unfilled and filled curves, respectively. $E_g = E_{\text{LUMO}} - E_{\text{HOMO}}$ is the gap between the valence and bipolaronic bands.

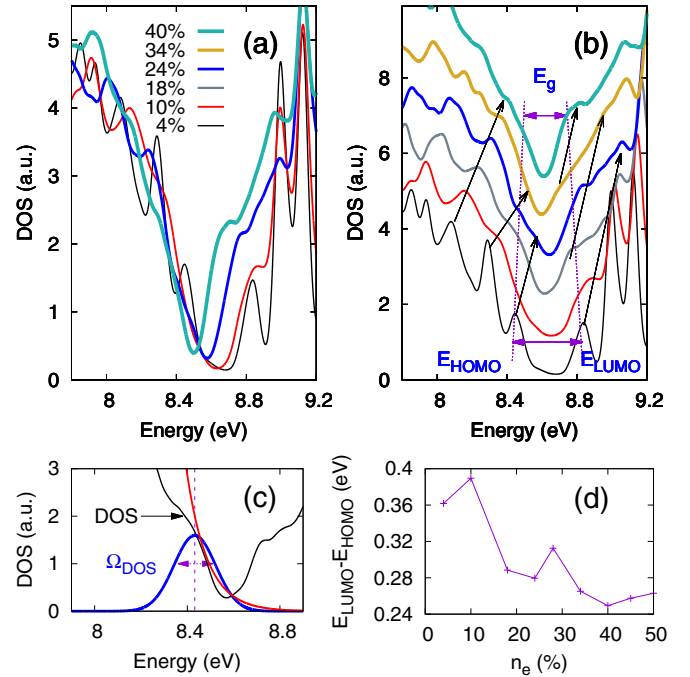


FIG. 3. (a),(b) DOS of (poly)crystalline PEDOT for different carrier concentrations n_e [(b) is the same as (a), but curves are vertically shifted for clarity]. Arrows in (b) point to successive bumps vanishing in the valence band and growing in the bipolaronic band as n_e is increased. Dotted lines indicate the position of the calculated E_{HOMO} and E_{LUMO} . (c) Fitting the Gaussian and exponential models to the calculated DOS for a representative charge density $n_e = 10\%$; a broadening of the fitted Gaussian DOS, $\Omega_{\text{DOS}} = 0.1$ eV, is indicated. (d) Dependence $E_g = E_{\text{LUMO}} - E_{\text{HOMO}}$ extracted from (b).

is worth mentioning that the electronic density is primarily localized at carbon atoms of the backbones.

Let us now turn to the electronic structure of polycrystalline PEDOT film focusing on bipolaron and valence bands. (Because the bipolarons represent holes, the transport in the system is due to hopping of bipolarons via the states in the valence band.) For a given concentration n_e , the DOS is obtained by averaging over many DOS of individual crystallites with different counterions distribution (sample realization). Figure 3 shows that the gap E_g between the bipolaron and valence band closes as the carrier concentration increases. (The gaps for the polycrystallite and E_{HOMO} and E_{LUMO} are calculated by averaging the corresponding values for individual crystallites for the same ensembles as used for the DOS calculations). The gap decreases by a factor of two when the carrier concentration is increased from 4% to 40%. Note that the gap between the bipolaron band and the conduction band completely closes already at $n_e = 10\%$. The density of states in the gap increases drastically (by a factor of 10) when the carrier concentration increases to 40%. These features of the band structure of polycrystalline PEDOT can be easily understood from the above analysis of the DOS for individual crystallites. Indeed, when the concentration increases, the bipolaron band widens as more states are pulled into it, which results in the decrease of the gap between the bipolaron and valence bands and closing the gap between the

bipolaron and conduction bands. A drastic increase of the DOS in the gap between the bipolaron and valence bands is related to the states emerging in the gap due to a disordered character of a potential landscape, as discussed above in Figs. 2(b) and 2(c).

Another pronounced feature of the DOS of (poly)crystallite PEDOT is its nonmonotonous character showing the presence of bumps and shoulders. The bumps/shoulders in the DOS can be attributed to the manifestation of the shell structure of individual crystallites, which has the same origin as the shell structure of atoms or few-electron quantum dots [35]. Arrows in Fig. 3(b) show an evolution of three representative bumps in the valence and the conduction band: the bumps in the valence band gradually disappear, whereas the bumps in the bipolaron band grow as the charge concentration increases. This behavior, as discussed above, is caused by moving states from the valence and conduction bands into the bipolaron band. Note that the presence of the bumps in the DOS leads to a nonmonotonic dependence of E_g as a function of the charge density, as shown in Fig. 3(d).

Our findings revealing the bumpy structure in the DOS can explain the experimental results showing the nonmonotonic behavior of the DOS in PEDOT and related polymers as revealed in studies using the ultraviolet photoelectron spectroscopy [36], conductivity and the Seebeck coefficient [37], and by cyclic voltammetry [38].

Figure 3(c) shows a comparison of the calculated DOS with commonly utilized Gaussian and exponential models of the DOS in conducting polymers. Apparently, the calculated DOS is described by neither Gaussian nor exponential dependence because of its bump structure and because it is essentially nonzero in the gap, as discussed above. In addition, the calculated DOS changes as n_e varies, a fact which is disregarded in the commonly used models of the DOS [13]. Despite the not strictly monotonic character of the DOS, we can still extract a rough estimate of the broadening, $\sigma_{DOS} \approx 0.1$ eV [see Fig. 3(c)], which is in good agreement with the corresponding value extracted from the experiments [12,14].

Let us now discuss the electron localization in the crystallites. It is measured by the inverse participation ratio defined as $IPR_i = \sum_j |C_{ij}|^4 / [\sum_j |C_{ij}|^2]^2$, where C_{ij} are the expansion coefficients of the wave function at the site j for the i th molecular orbital [39]; see Fig. 4. As follows from the definition of IPR, if an electron state is delocalized over m atoms, its $IPR \approx \frac{1}{m}$. To understand the calculated IPR, we first note that for a bipolaron in a single chain, $IPR_{bp} = 0.054$, which corresponds to the delocalization over six monomer units (i.e., over $m \approx 24$ carbon atoms in a backbone; see Fig. 5). The case of $n_e = 4\%$ in Fig. 4 corresponds to one bipolaron in a whole crystallite. The calculated IPR for states in the bipolaronic band ($E > E_{LUMO}$) is smaller than IPR_{bp} , which means that π - π stacking enhances the delocalization of the bipolaron. As the charge concentration increases, the delocalization of bipolarons further increases, which we attribute to the effect of electron interaction leading to the Coulomb repulsion between bipolarons. For $n_e = 34\%$, bipolarons are delocalized over $m \approx \frac{1}{IPR} \approx 50$ atoms. Note that a typical state is delocalized over more than one chain in a crystallite, which is illustrated in the inset to Fig. 4.

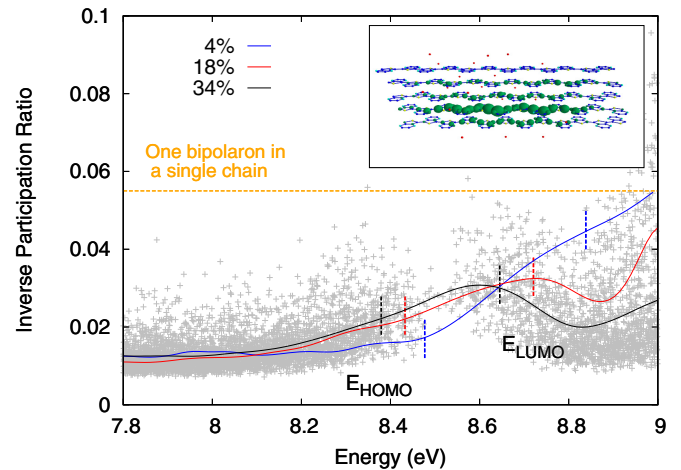


FIG. 4. Inverse participation ratio (IPR) for different carrier concentrations $n_e = 4\%$, 18% , and 34% . The curves are averaged; gray dots represent data for $n_e = 34\%$ for 1000 configurations. Dashed lines indicate the averaged highest occupied molecular orbital (HOMO) and lowest unoccupied molecular orbital (LUMO) energy for each case. A horizontal line shows the IPR for one bipolaron on a single chain. The inset shows the electronic localization of a bipolaron state in a representative crystallite for $n_e = 34\%$.

These findings combined with the behavior of the DOS discussed above support the conclusions of Bubnova *et al.* [4] concerning the possibility of semimetallic behavior in highly doped PEDOT polymers. Indeed, we find that when the carrier concentration increases, the band structure gradually evolves from the insulating to the semimetallic character, showing a collapse of the gap between the bipolaron and valence bands with a drastic increase of the DOS in it. It is also worth noting that for high electron densities, the band structure exhibits a characteristic V-shaped profile typical of semimetals. These changes in the band structure are accompanied by a formation of a network of strongly delocalized and therefore highly overlapping current-carrying states in the valence band that can efficiently transport holes.

We stress that in our study, we calculate the electronic structure and do not focus on transport properties of the system at hand. The latter are strongly dependent not only on the DOS, but on the morphology of the system, in particular, how efficient individual crystallites are connected by percolative transport paths. As crystallites are believed to be embedded into an amorphous phase, the conductivity of the (poly)crystalline system can be limited by hopping transport in the amorphous phase. We speculate that the PEDOT systems exhibiting semimetallic behavior in Ref. [4] correspond to morphologies where the amorphous regions no longer represent the limiting factor governing the conductivity.

Finally, it is noteworthy that the insulator to semimetallic transition in PEDOT can be defined as disorder driven because it takes place when the concentration of disorder (i.e., randomly distributed counterions oxidizing the polymer) increases. This is apparently strikingly different from the case of metals or two-dimensional electron gases (2DEGs), where instead the disorder drives the system from metallic into an insulating state. It should be noted, however, that the increase of the disorder concentration in conducting polymers is accompa-

nied by an increase of the carrier density, whereas in the metals or 2DEG systems, the density is not affected by disorder.

IV. CONCLUSIONS

Among all conducting polymers, PEDOT or poly(3,4-ethylenedioxythiophene) has a special place because it plays the same role in organic electronics as silicon in the semiconductor industry. Realistic PEDOT films are neither periodic crystals nor completely amorphous structures. Because of the complexity of their morphology, the microscopic understanding of the electronic structure and the density of states are still missing. In the present work, we account for the nature of charge carriers and complexity of morphology in realistic PEDOT films from the angstrom to the nanometer scale and provide a microscopic description of its electronic structure using multiscale modeling employing *ab initio*, molecular dynamics, and semiempirical calculations. The method developed in this work is general and can be applied to study the electronic structure of other conducting polymers. We start with molecular dynamics simulations and use available experimental data to develop a model for PEDOT morphology. We then develop a semiempirical approach capable of calculating the electronic properties of a system consisting of thousands of atoms, with parameters of this approach being obtained from the *ab initio* calculations. Using the developed methodology, we calculate the electronic structure of realistic PEDOT. We show that when the charge carrier concentration increases, the character of the DOS gradually evolves from insulating to semimetallic, exhibiting a collapse of the gap between the bipolaron and valence bands with a drastic increase of the DOS between these bands. The origin of the observed behavior is attributed to the effect of randomly located counterions giving rise to the states in the gap. Our findings support the conclusion of a recent experiment by Bubnova *et al.* [4] on semimetallic behavior of highly doped PEDOT polymers. It is noteworthy that the mechanism of the semimetallic transition in PEDOT is strikingly different from the one of metals or two-dimensional electron gases. In the latter case, the disorder drives the system into an insulating state. In contrast, in PEDOT, the disorder in the system (i.e., randomly distributed counterions oxidizing the polymer) drives the system into a semimetallic state. A pronounced feature of the DOS of realistic PEDOT is its nonmonotonous character showing the presence of bumps and shoulders. The bumpy structure in the calculated DOS can explain the experimental results showing the nonmonotonic behavior of the DOS in PEDOT and related polymers as revealed in studies using the ultraviolet photoelectron spectroscopy [35], conductivity and the Seebeck coefficient [36], and by cyclic voltammetry [37]. We find that the calculated DOS in a doped PEDOT is not well described by Gaussian or exponential dependencies (often used in phenomenological models) because of its bump structure and because it is essentially nonzero in the gap.

ACKNOWLEDGMENTS

This work was supported by the Swedish Energy Agency, Knut and Alice Wallenberg Foundation (The Tail of the Sun), and Carl Tryggers Foundation. M.L. thanks SeRC for funding.

X.C. thanks the European Research Council (ERC Starting Grant No. 307596) and the Advanced Functional Material Center at Linköping University. The computations were performed on resources provided by the Swedish National Infrastructure for Computing (SNIC) at NSC.

APPENDIX A: CLASSICAL MOLECULAR DYNAMICS

Classical molecular dynamics simulations were performed in order to obtain realistic morphology and crystal configurations of PEDOT with tosylate (TOS) molecules serving as counterions. Polymer chains of a length of 12 monomers were used in the calculations and a charge carrier concentration was set to 33% (corresponding to a pristine PEDOT). A number of positive charges on the PEDOT chains was equal to the number of negative TOS counterions. The partial charges per atom in the PEDOT chains were calculated using the *ab initio* DFT functional WB97XD [40] with the 6-31 + g(d) [41] basis set and fitting to electrostatic potential (ESP) [42] as implemented in the Gaussian suite [43]. PEDOT chains and TOS molecules were solvated in water with a concentration of water 13% w.t. All of the molecules were initially randomly placed in a solvent box and the system was described by the all-atom force field GAFF and a model SPC/E for water. The system was then minimized and equilibrated for 20 ns production run [44,45] using the LAMMPS package [46]. As a result, the crystal nucleation takes places in the solution such that well-defined crystallites of PEDOT:TOS are obtained, as shown in Fig. 1 of the main text. Counterion molecules are found to be both side oriented to the PEDOT chains and situated above and below the upper and lower chains in the crystallite.

APPENDIX B: SEMIEMPIRICAL MODEL: MINIMIZATION OF THE TOTAL ENERGY

The Hamiltonian given by Eq. (1) for π -electrons defines a tight-binding lattice consisting of $N = 420$ atomic sites. (A crystallite is composed of five PEDOT chains, each consisting of 12 monomers. Each monomer contains seven π -electrons corresponding to four C atoms of the backbone, two O atoms, and one S atom.) We first diagonalize the Hamiltonian (1) and calculate the expansion coefficients C_{nl} of the wave function of the l th molecular orbital at the atomic site n . We then compute the total energy corresponding to the Hamiltonian (1) as follows [24,32]:

$$\begin{aligned}
 E_T = & \sum_{n\sigma} \left[\varepsilon_n P_{nn}^\sigma - \sum_m t_{nm} P_{nm}^\sigma - \sum_{m'} t_{nm'}^{\pi-\pi} P_{nm'}^\sigma \right] \\
 & + \sum_{nm} K_{nm} (u_{n,m} - u_{n,m}^0 - \alpha^{-1}) \\
 & + \frac{1}{2} \sum_{nm\sigma\sigma'} V_{nm} (P_{nn}^\sigma P_{mm}^{\sigma'} - P_{nn}^\sigma P_{mm}^{\sigma'} \delta_{nm} \delta_{\sigma\sigma'}) \\
 & + \sum_n V_n^{\text{ion}} P_{nn}^\sigma,
 \end{aligned} \tag{B1}$$

where P_{nm}^σ is the element of the density matrix given by

$$P_{nm}^\sigma = \sum_l n_l^\sigma C_{nl}^\sigma C_{ml}^\sigma, \tag{B2}$$

with $n_l^\sigma = 0, 1$ being the occupation number of the (l, σ) th orbital. Minimization of the total energy with respect to u_{nm} is done for all sites (n, m) in the Hamiltonian (1) according to $\partial E_T / \partial u_{nm} = 0$, which leads us to the following self-consistent solution for the ground-state geometry (i.e., bond-length distances u_{nm}),

$$u_{nm} = u_{nm}^0 - 2 \sum_{\sigma} P_{nm}^{\sigma} / \beta + O(\partial P_{nm}^{\sigma} / \partial u_{nm}). \quad (\text{B3})$$

This procedure (including the diagonalization of the Hamiltonian) is repeated until the self-consistent solution for the ground-state geometry corresponding to a predefined convergence condition is reached. (The convergence is assumed to be achieved when the difference in the bond length u_{nm} for two consecutive steps is less than 10^{-5} Å.) Finally, the density of states is calculated for the ground-state geometry by using a standard tridiagonalization procedure.

The last term in Eq. (B3) contains derivatives of the density matrix elements. Since these derivatives are supposed to be zero once the system has reached the equilibrium, the last term in Eq. (B3) can be safely neglected [47]. Note that a contribution of the terms corresponding to interlayer hopping as well as to electron-electron and electron-ion interactions is not included in Eq. (B3) because they are much smaller than the terms corresponding to intralayer hopping and electron-phonon coupling.

APPENDIX C: PARAMETRIZATION OF THE SEMI-EMPIRICAL HAMILTONIAN USING DFT CALCULATIONS

1. DFT calculations

The DFT calculations are performed using the GAUSSIAN (G09) package [43]. Structural optimization of the PEDOT chains was done with hybrid exchange-correlation functional B3PW91 [48,49] and basis set 6-31 + G(d) [41], with diffuse and polarization functions on all atoms. The empirical dispersion correction is added by the D3 version of Grimme's dispersion with Becke-Johnson damping [50]. In our study, we use Cl_3^- as counterions since they do not form covalent bonds [51] to the PEDOT backbone and charge transfer from PEDOT backbone to Cl_3^- counterion is close to unity (0.9e). The Cl_3^- counterion is relatively small in comparison to other counterions (TOS , ClO_4^- , NO_3^-), which allows calculations of doped PEDOT within a reasonable amount of computational resources and time. We also performed calculations with the above-mentioned counterions (TOS , ClO_4^- , NO_3^-) and found that the calculated electronic structure is practically insensitive to the choice of a counterion.

2. Parametrization of the Hamiltonian

The parametrization of the semiempirical Hamiltonian, given by Eq. (1), using the DFT calculations was performed in three consecutive steps:

First step. Single undoped chain: determination of t_0 , α , and β . We start with a single undoped PEDOT chain to parametrize the values of the hopping integral t_0 and the electron-phonon coupling constants α and β in Eqs. (1)–(3). As a reference for the parametrization, we use the experimental energy gap

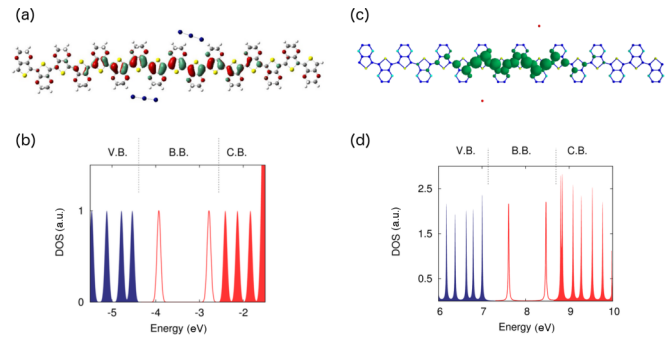


FIG. 5. A comparison of DFT and semiempirical calculations (left and right panels, respectively) for a single PEDOT chain with one bipolaron in a presence of counterions. (a),(c) Visualization of a molecular orbital for the lowest bipolaron state. (b),(d) Band diagram of the PEDOT chain. The occupied and unoccupied electronic states are denoted in red and blue. For visualization purposes, each level is plotted as a Lorentzian with a finite width. Unfilled Lorentzians correspond to the bipolaron states. V.B., B.B., and C.B. correspond to the valence, bipolaron, and conduction bands, respectively. Cl_3^- and $(-e)$ point charges were used as the counterions in DFT and semiempirical calculations, respectively. The PEDOT chain consists of 16 monomers.

$E_g = 1.7$ eV and the conjugated bond lengths 1.34 and 1.42 Å in the aromatic PEDOT backbone as obtained from our DFT calculations and reported previously in the literature [27,52].

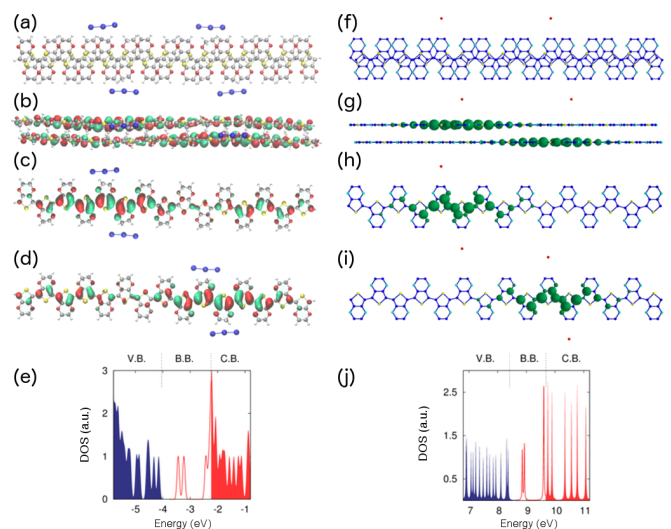


FIG. 6. A comparison of DFT and semiempirical calculations (left and right panels, respectively) for two π - π stacked PEDOT chains with two bipolarons in the presence of counterions. (a),(f) Position of the chains and counterions; (b)–(d) and (g)–(i) Visualization of a molecular orbital for the lowest bipolaron state. [(b),(g) is a side view and (c),(d) and (h),(i) is a top view for the upper and lower chains.] (e),(j) band diagram of a PEDOT chain with one bipolaron. The occupied and unoccupied electronic states are denoted in red and blue. For visualization purposes, each level is plotted as a Lorentzian with a finite width. Unfilled Lorentzians correspond to the bipolaron states. V.B., B.B., and C.B. correspond to the valence, bipolaron, and conduction bands, respectively. Cl_3^- and $(-e)$ point charges were used as the counterions in DFT and semiempirical calculations, respectively. The PEDOT chain consists of 15 monomers.

We obtain the following values: $t_0 = 2.46 \text{ \AA}^{-1}$, $\alpha = 2.9 \text{ \AA}^{-1}$, $\beta = 7.714 \text{ \AA}^{-1}$, which are close to the corresponding values reported for related polymers such as polythiophene [24]. For the on-site energies, we use values previously published in the literature [34], $\varepsilon_{0i}^O = -5.46 \text{ eV}$, $\varepsilon_{0i}^S = -2.85 \text{ eV}$, and $\varepsilon_{0i}^C = 0 \text{ eV}$, for the oxygen (O), sulfur (S), and carbon (C) atoms, respectively. Note that parameters t_0 , α , and β are rather insensitive to the choice of the on-site energies for oxygen and sulfur atoms. This is because for these values of ε_{0i} the molecular orbitals are primarily localized on the carbon atoms; see Figs. 5 and 6 for illustration.

Second step. Single doped chain: determination of γ (intrachain) and U_0 . For the determination of the parameters describing the Coulomb interaction and screening within the same chain, we consider a single chain containing one bipolaron (i.e., the total charge $+2e$) in the presence of two negative counterions. Figures 5(a) and 5(c) show the molecular orbital for the lowest bipolaron state and the band structure for a PEDOT chain according to the DFT calculations. We choose the screening parameter γ and the on-site Coulomb interaction U_0 to match the energy distance between the highest occupied molecular orbital (HOMO) and the lowest bipolaron state, and the energy distance between the two bipolaron states, as well as to match the localization length of the bipolaron in the chain. The best agreement is achieved for $U_0 = 2.2 \text{ eV}$ and $\gamma = 0.65$, which is illustrated in Figs. 5(b) and 5(d), showing the results of the corresponding semiempirical calculations.

Third step. Two π - π stacked chains: determination of γ (interchain) and $t_0^{\pi-\pi}$. For the determination of the interchain

screening γ and the interchain hopping integral $t_0^{\pi-\pi}$, we consider two π - π stacked chains with a total charge $+4e$ in the presence of four counterions, as illustrated in Figs. 6(a) and 6(f). We assume that the values of the parameters determined at the previous steps can be used for the π - π stacking structure as well. Figures 6(b)–6(d) show the molecular orbital of the lowest bipolaron state and the band structure for two π - π stacked chains according to the DFT calculations. The interchain coupling causes a hybridization of the bipolaronic state, leading to its localization in both chains. The parameters γ (interchain) and $t_0^{\pi-\pi}$ are determined by matching the energy distance between the HOMO and the lowest bipolaron state, and by matching the energy distance between bipolaron states. A stacking configuration used in the semiempirical calculations was obtained from the geometry optimization given by the DFT calculations. The best agreement is achieved for γ (interchain) = 1.2 and $t_0^{\pi-\pi} = 0.32 \text{ eV}$; see Figs. 6(f)–6(j). It is noteworthy that the interchain coupling $t_0^{\pi-\pi}$ mostly influences the energy distance between the bipolaron states.

We conclude this section by noting that it might be possible to provide more elaborated parametrization schemes that could ensure even better agreement between the semiempirical and DFT calculations. It should be stressed, however, that different functionals used in the DFT calculations (e.g., hybrid functional vs range-separated ones) do not lead to the same results concerning, e.g., the band gap, the localization length for bipolarons, etc. Thus, because of this ambiguity of the DFT calculations, the more elaborate parametrization scheme would not necessarily lead to more accurate parameters of the semiempirical Hamiltonian.

-
- [1] P. A. Levermore, L. Chen, X. Wang, R. Das, and D. D. C. Bradley, *Adv. Mater.* **19**, 2379 (2007).
- [2] S. H. Kim, K. Hong, W. Xie, K. H. Lee, S. Zhang, T. P. Lodge, and C. D. Frisbie, *Adv. Mater.* **25**, 1822 (2013).
- [3] A. Malti *et al.*, *Adv. Sci.* **3**, 1500305 (2016).
- [4] O. Bubnova *et al.*, *Nat. Mater.* **13**, 190 (2014).
- [5] N. Kim, H. Kang, J.-H. Lee, S. Kee, S. H. Lee, and K. Lee, *Adv. Mater.* **27**, 2317 (2015).
- [6] H. Shi, C. Liu, Q. Jiang, and J. Xu, *Adv. Electron. Mater.* **1**, 1500017 (2015).
- [7] A. Elschner, S. Kirchmeyer, W. Lovenich, U. Merker, and K. Reuter, *PEDOT: Principles and Applications of an Intrinsically Conductive Polymer* (CRC, Boca Raton, FL, 2010).
- [8] O. Bubnova, Z. U. Khan, A. Malti, S. Braun, M. Fahlman, M. Berggren, and X. Crispin, *Nat. Mater.* **10**, 429 (2011).
- [9] T. Park, C. Park, B. Kim, H. Shin, and E. Kim, *Energy Environ. Sci.* **6**, 788 (2013).
- [10] N. Massonnet, A. Carella, A. de Geyer, J. Faure-Vincent, and J.-P. Simonato, *Chem. Sci.* **6**, 412 (2014).
- [11] Q. Wei, M. Mukaida, K. Kirihara, Y. Naitoh, and T. Ishida, *Materials* **8**, 732 (2015).
- [12] G. Kim and K. P. Pipe, *Phys. Rev. B* **86**, 085208 (2012).
- [13] S. D. Baranovskii, *Phys. Status Solidi B* **251**, 487 (2014).
- [14] S. Ihnatsenka, X. Crispin, and I. V. Zozoulenko, *Phys. Rev. B* **92**, 035201 (2015).
- [15] H. Bässler, *Phys. Status Solidi B* **175**, 15 (1993).
- [16] W. R. Salaneck, R. H. Friend, and J. L. Brédas, *Phys. Rep.* **319**, 231 (1999).
- [17] O. Bubnova and X. Crispin, *Energy Environ. Sci.* **5**, 9345 (2012).
- [18] A. Ugur, F. Katmis, M. Li, L. Wu, Y. Zhu, K. K. Varanasi, and K. K. Gleason, *Adv. Mater.* **27**, 4604 (2015).
- [19] N. Kim, B. H. Lee, D. Choi, G. Kim, H. Kim, J.-R. Kim, J. Lee, Y. H. Kahng, and K. Lee, *Phys. Rev. Lett.* **109**, 106405 (2012).
- [20] F.-C. Hsu, V. N. Prigodin, and A. J. Epstein, *Phys. Rev. B* **74**, 235219 (2006).
- [21] A. Dkhissi, D. Beljonne, R. Lazzaroni, F. Louwet, L. Groenendaal, and J. L. Brédas, *Int. J. Quantum Chem.* **91**, 517 (2003).
- [22] N. Zamoshchik and M. Bendikov, *Adv. Funct. Mater.* **18**, 3377 (2008).
- [23] F. C. Lavarda, M. C. dos Santos, D. S. Galvão, and B. Laks, *Phys. Rev. B* **49**, 979 (1994).
- [24] D. Giri and K. Kundu, *Phys. Rev. B* **53**, 4340 (1996).
- [25] A. Lenz, H. Kariis, A. Pohl, P. Persson, and L. Ojamae, *Chem. Phys.* **384**, 44 (2011).
- [26] E.-G. Kim and J.-L. Brédas, *J. Am. Chem. Soc.* **130**, 16880 (2008).
- [27] W. Shi, T. Zhao, J. Xi, D. Wang, and Z. Shuai, *J. Am. Chem. Soc.* **137**, 12929 (2015).
- [28] J. O. Oelerich, D. Huemmer, and S. D. Baranovskii, *Phys. Rev. Lett.* **108**, 226403 (2012).

- [29] T. Takano, H. Masunaga, A. Fujiwara, H. Okuzaki, and T. Sasaki, *Macromolecules* **45**, 3859 (2012).
- [30] C. M. Palumbiny, F. Liu, T. P. Russell, A. Hexemer, C. Wang, and P. Müller-Buschbaum, *Adv. Mater.* **27**, 3391 (2015).
- [31] A. J. Heeger, S. Kivelson, J. R. Schrieffer, and W. P. Su, *Rev. Mod. Phys.* **60**, 781 (1988).
- [32] S. Stafström, *Phys. Rev. B* **43**, 9158 (1991).
- [33] M. Chandross, S. Mazumdar, M. Liess, P. A. Lane, Z. V. Vardeny, M. Hamaguchi, and K. Yoshino, *Phys. Rev. B* **55**, 1486 (1997).
- [34] A. L. Botelho, Y. Shin, J. Liu, and X. Lin, *PLoS ONE* **9**, e86370 (2014).
- [35] S. M. Reimann and M. Manninen, *Rev. Mod. Phys.* **74**, 1283 (2002).
- [36] M. P. de Jong, A. W. D. van der Gon, X. Crispin, W. Osikowicz, W. R. Salaneck, and L. Groenendaal, *J. Chem. Phys.* **118**, 6495 (2003).
- [37] O. Bubnova, M. Berggren, and X. Crispin, *J. Am. Chem. Soc.* **134**, 16456 (2012).
- [38] B. D. Paulsen and C. D. Frisbie, *J. Phys. Chem. C* **116**, 3132 (2012).
- [39] M. Linares, M. Hultell, and S. Stafström, *Synth. Met.* **159**, 2219 (2009).
- [40] Y.-S. Lin, G.-D. Li, S.-P. Mao, and J.-D. Chai, *J. Chem. Theory Comput.* **9**, 263 (2013).
- [41] R. Krishnan, J. S. Binkley, R. Seeger, and J. A. Pople, *J. Chem. Phys.* **72**, 650 (1980).
- [42] U. C. Singh and P. A. Kollman, *J. Comput. Chem.* **5**, 129 (1984).
- [43] M. J. Frisch *et al.*, *computer code GAUSSIAN 09*, Revision D.01 (Gaussian Inc., Wallingford, CT, 2009).
- [44] F. Liu, Y. Gu, J. W. Jung, W. H. Jo, and T. P. Russell, *J. Polym. Sci. B Polym. Phys.* **50**, 1018 (2012).
- [45] K. Harano, S. Okada, S. Furukawa, H. Tanaka, and E. Nakamura, *J. Polym. Sci. Part B: Polym. Phys.* **52**, 833 (2014).
- [46] S. Plimpton, *J. Comput. Phys.* **117**, 1 (1995).
- [47] S. Stafström and K. A. Chao, *Phys. Rev. B* **30**, 2098 (1984).
- [48] A. D. Becke, *J. Chem. Phys.* **98**, 5648 (1993).
- [49] J. P. Perdew, K. Burke, and Y. Wang, *Phys. Rev. B* **54**, 16533 (1996).
- [50] S. Grimme, S. Ehrlich, and L. Goerigk, *J. Comput. Chem.* **32**, 1456 (2011).
- [51] U. Salzner, *J. Chem. Theory Comput.* **3**, 1143 (2007).
- [52] E. E. Havinga, C. M. J. Mutsaers, and L. W. Jenneskens, *Chem. Mater.* **8**, 769 (1996).